

Monitoring Topographic Changes in a Periglacial High-mountain Face using High-resolution DTMs, Monte Rosa East Face, Italian Alps

Luzia Fischer,^{1*} Henri Eisenbeiss,² Andreas Käb,³ Christian Huggel¹ and Wilfried Haeberli¹

¹ Glaciology, Geomorphodynamics and Geochronology, Department of Geography, University of Zurich, Switzerland

² Institute of Geodesy and Photogrammetry, ETH Zurich, Switzerland

³ Department of Geosciences, University of Oslo, Norway

ABSTRACT

This paper describes a remote sensing-based approach for detailed topographic investigations in steep periglacial high-mountain faces. The study was conducted at one of the highest periglacial rock faces in the European Alps, the permafrost-affected and partially glacierised east face of Monte Rosa. Strongly increased rock and ice avalanche activity on this rock wall has caused major topographic change in recent decades. A time series of high-resolution digital terrain models (DTMs) with a 2-m resolution was produced from digital aerial photogrammetry for 1956, 1988 and 2001 and from airborne LiDAR for 2005 and 2007. The DTM comparisons reveal a total volume loss of permafrost-affected bedrock and glacier ice of more than $20 \times 10^6 \text{ m}^3$ over the past 50 years, with the majority of the loss since 1988. Analysis of all unstable areas and detachment zones showed that the sequence of the main slope failures is spatially connected and that there is coupling between permafrost bedrock instability and the condition of adjacent hanging glaciers. Copyright © 2011 John Wiley & Sons, Ltd.

KEY WORDS: rock avalanche; ice avalanche; LiDAR; slope instability; mountain permafrost; Topographic changes; Periglacial rock wall; high-resolution DTM; Photogrammetry

INTRODUCTION

Atmospheric warming over the past century has caused pronounced effects in the periglacial and glacial belts of high-mountain areas (IPCC, 2007). Changes in the distribution and temperature of permafrost and surface ice have affected the stability of steep high-mountain faces by influencing the thermal and stress fields in both rock and ice, their geotechnical properties and their groundwater regimes (Haeberli *et al.*, 1997; Davies *et al.*, 2001; Harris *et al.*, 2009; Fischer *et al.*, 2010). The coexistence of permafrost and hanging glaciers in a high-mountain face can give rise to deep-seated geothermal anomalies and extremely complex hydrological/hydraulic conditions (Wegmann *et al.*, 1998; Haeberli *et al.*, 2004; Huggel, 2009). Reduced slope stability may result in natural hazards such as rock avalanches, ice avalanches, or combined events. A number of these mass movement events, with volumes between 10^6 and 10^7 m^3 , have occurred over the

past few decades in mountain belts located in the European Alps (e.g. Barla *et al.*, 2000; Noetzli *et al.*, 2003; Cola, 2005; Oppikofer *et al.*, 2008; Fischer, 2009), Canada and Alaska (e.g. Evans and Clague, 1994; Geertsema *et al.*, 2006), the Caucasus (Huggel *et al.*, 2005) and New Zealand (e.g. Cox and Allen, 2009; Allen *et al.*, 2009).

Major obstacles to a better understanding of slope instability processes on periglacial high-mountain rock walls include the difficulty of accessing these sites directly and the lack of detailed topographic data. Digital terrain models (DTMs) from remotely sensed data represent a good tool for topographic and morphometric analyses and DTM time series can be very effective in accurately defining temporal change in terrain surfaces (Käb, 2002; Baldi *et al.*, 2002). However, the generation of detailed DTMs for steep high-mountain flanks is complicated by the steepness and poor image contrast in glaciated parts. For tasks requiring ground resolution and accuracy at a metre scale, aerial photographs and light detection and ranging (LiDAR) data are appropriate for DTM generation (Baltsavias *et al.*, 2001; Buchroithner, 2002). Digital photogrammetry based on aerial images can also be a valuable source of data for long-term topographic change (Baltsavias, 1999; Käb, 2008). Terrestrial and airborne laser scanning, in turn, is a

* Correspondence to: Luzia Fischer, Geological Survey of Norway (NGU), Leiv Eirikssons vei 39, 7040, Trondheim, Norway.
E-mail: luzia.fischer@ngu.no

Contract/grant sponsor: Swiss National Science Foundation 200021-111967.

rapidly emerging and highly promising tool for acquiring high-resolution topographic information (e.g. Ruiz *et al.*, 2004; Rabatel *et al.*, 2008; Oppikofer *et al.*, 2008). Some projects have already taken advantage of combining digital photogrammetry and LiDAR for multi-temporal topographic analyses of rock walls (Lim *et al.*, 2005; Dewitte *et al.*, 2008), as well as for the detection of changes in valley glaciers (Baltsavias *et al.*, 2001). However, the combination of the two techniques has not previously been applied to steep permafrost-affected and glacierised high-mountain rock walls.

The main objective of this study was to establish a methodology to investigate topographic changes in steep periglacial rock walls in detail and over a long time period. To achieve this goal, a time series of high-resolution DTMs from high-precision digital aerial photogrammetry and airborne LiDAR was developed. Temporal and spatial changes in surface topography were evaluated to assess terrain changes quantitatively over the past 50 years to enhance understanding of periglacial and glacial processes, and especially slope instability.

STUDY AREA

The case study area comprised the steep east face of Monte Rosa (45°56'N, 7°53'E, Figure 1), which is amongst the highest faces in the European Alps (2200–4600 m asl).

Surface temperature measurements and permafrost modelling based on regionally calibrated empirical-statistical models have shown that large parts of the face are affected by permafrost (Zraggen, 2005; Fischer *et al.*, 2006) (Figure 1). This is believed to have experienced changes in extent and temperature during the 20th century, as elsewhere in the European Alps (Harris *et al.*, 2009; Gruber and Haeberli, 2007). Steep hanging glaciers and firn/ice fields also cover large parts of the wall and their extent and thickness have diminished at unprecedented rates over the past few decades (Haeberli *et al.*, 2002; Kääb *et al.*, 2004; Fischer *et al.*, 2006).

Since about 1990, new slope instabilities have developed within the altitudinal permafrost belt in bedrock areas and in relation to hanging glaciers (Kääb *et al.*, 2004; Fischer *et al.*, 2006). Frequent small-scale as well as several large-scale rock and ice avalanches and debris flow events have led to significant topographic change. A major rock/ice avalanche was reported in summer 1990 and several rock and ice avalanche events followed, detaching large parts of a hanging glacier and underlying bedrock. In August 2005, an ice avalanche with a volume of more than $1 \times 10^6 \text{ m}^3$ occurred, and in April 2007 a rock avalanche of $0.2 \times 10^6 \text{ m}^3$ detached from the uppermost part of the face where continuous permafrost is expected. The volume of the 2005 ice avalanche is among the largest documented in the European Alps over the past 100 years. Such slope failures can trigger far-reaching chain reactions, especially in combination with the temporary supraglacial lake 'Effimero' (Figure 1) which developed in connection with

a surge-type behaviour of the Belvedere Glacier in September 2001 and reached a maximum volume of $3 \times 10^6 \text{ m}^3$ in the following two summers (Haeberli *et al.*, 2002; Kääb *et al.*, 2004; Tamburini and Mortara, 2005). Rock and ice avalanches from the Monte Rosa east face into the full lake could have triggered a catastrophic outburst with an extended range of destruction downstream. In view of the ongoing or even enhanced atmospheric warming, it is very likely that slope failures from bedrock and hanging glaciers on the Monte Rosa east face will continue to be a source of hazards for the populated downstream valley region.

DATA SETS

A combination of optical remote sensing techniques was used for the generation of multi-temporal DTMs of the Monte Rosa east face (Table 1).

Analogue Aerial Images

Analogue aerial images of the Monte Rosa east face exist from about 1950 onwards and have been taken repeatedly at intervals of 5 to 10 years by both the Swiss Federal Office of Topography (swisstopo) and the Italian Istituto Geografico Militare. Aerial images from 1956, 1988 and 2001 (swisstopo, Table 1) were selected based on the goals of a well-distributed chronological sequence, good image quality with little snow coverage and preferably limited distortion. The quality of the aerial images varied significantly between 1956 and 2001, with more coarse-grained images in 1956 (Züblin *et al.*, 2008). In addition, large distortions are present due to the vertical acquisition, the geometry and steepness of the Monte Rosa east face, and strongly varying scales within the individual images due to elevation differences exceeding 2000 m over a horizontal distance of 3 km. The black and white aerial images were scanned at 10- μm resolution using a Vexcel photogrammetric scanner (Vexcel Imaging GmbH, Graz, Austria), resulting in a pixel size (i.e. horizontal resolution on the ground) of 6 to 28 cm (Table 1).

Terrestrial photographs taken over several decades were also compiled. These images were used mainly for visual interpretation of terrain characteristics in combination with the DTMs.

LiDAR Data

Two airborne LiDAR data sets are available for the Monte Rosa east face. The first was collected by the Swissphoto Group using an aeroplane in 2005, and for the present study, a 6.5-km² area was extracted from the original 650 km². Data were acquired on parallel flight lines in an E-W direction and scanning was performed vertically. The LiDAR point cloud contains approximately 18.5×10^6 pt (Table 1) with a point density of 2–3 pt/m² and vertical

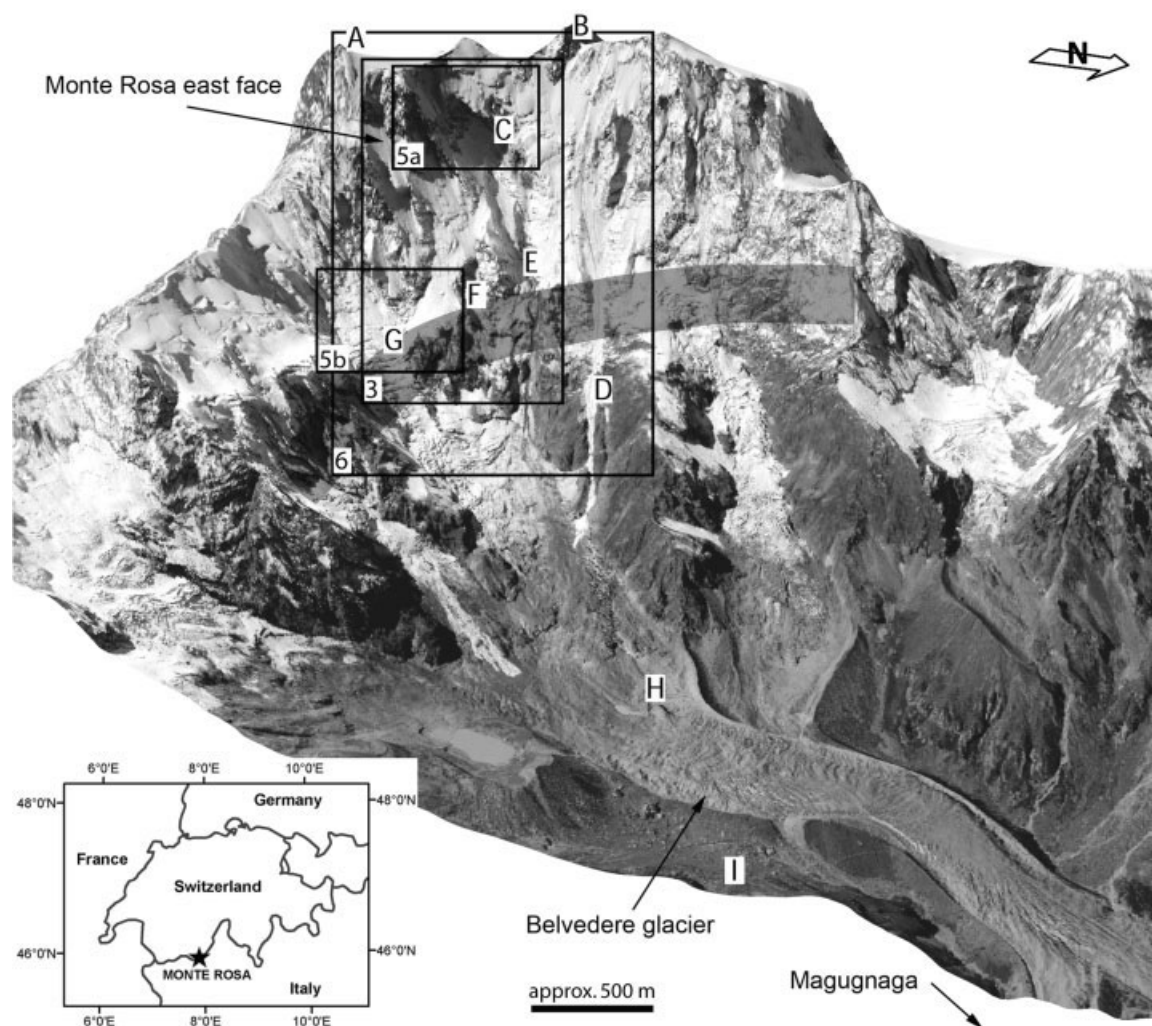


Figure 1 Oblique view on the Monte Rosa east face and the Belvedere glacier from the northeast. The synthesised view is developed from an orthophoto of 2005 and a photogrammetric DTM from 2001. The upper part of the face is assumed to be underlain by continuous permafrost, and the horizontal grey band indicates the approximate lower boundary of permafrost occurrence, where permafrost is presumed to be discontinuous. A = Signalkuppe; B = Dufourspitze; C = Parete Innominata; D = Marinelli Channel; E = Imsegg Channel; F = Zapparoli Channel; G = Monte Rosa Glacier; H = Lake Lago Effimero; I = alpine hut Zamboni. The rectangles show the extent of Figures 3, 5 and 6.

point accuracy better than 0.3 m (Luethy and Stengele, 2005).

In September 2007, LiDAR data and high-resolution oblique photographs were acquired from a helicopter using the Helimap system of the company UW + R SA (Vallet, 2007; Vallet and Skaloud, 2004). Data acquisition was done along 14 horizontal flight lines that were arranged parallel to each other but at different heights in order to cover the whole face. Scanning was performed almost perpendicularly to the rock wall, as the system is operated manually and can be tilted. The point cloud of this LiDAR data consists of 4.8×10^6 pt and covers a total area of 3 km^2 with a point density of $1 - 3 \text{ pt/m}^2$ and vertical point accuracy better than 0.2 m (Table 1; Skaloud *et al.*, 2005).

DATA-PROCESSING METHODS

Analogue Aerial Image Processing

Image Triangulation.

The generation of stereo-models was done with the Leica Photogrammetry Suite (LPS; Wang *et al.*, 2004). An image block was set up for each year, using three aerial images for 2001 and four aerial images for 1956 and 1988. The inner orientation of the scanned aerial images was carried out using the parameters from the camera calibration protocols from swisstopo.

In the next step, the outer orientation had to be calibrated for each image block to obtain a stereo-model. For the

Table 1 Date and main parameters of available optical data.

Date	Type of data	Camera/ sensor type	Quantity of data used	Focal length [mm]	Flying height (asl)	Image scale	¹ Pixel size = Ground resolution / ² Point density	Area of DTM produced
Sept 1956	Aerial images	Wild RC 5	4 images	115.26	5020 m	1:6000 to 1:23 000	¹ 6–23 cm	4 km ²
Sept 1988	Aerial images	Wild RC 10	4 images	153.37	6100 m	1:11 000 to 1:24 000	¹ 11–24 cm	25 km ²
Sept 2001	Aerial images	Wild RC 10	3 images	153.28	6700 m	1:16 000 to 1:28 000	¹ 16–28 cm	20 km ²
Autumn 2005	LiDAR (aeroplane based)	Optech ALTM3100	18.5 × 10 ⁶ pt	—	Not available	—	² 2–3 pt/m ²	6 km ²
Sept 2007	LiDAR (helicopter based)	Riegl LMS-Q240i-60	4.8 × 10 ⁶ pt	—	Various heights	—	² 1–3 pt/m ²	3 km ²

Note: Image scale is calculated with the ratio of the focal length divided by the flying height above the terrain. Abbreviations as given in the text.

reconstruction of the geometry of the block, LPS uses a one-step bundle adjustment for tie points and ground control points (GCPs). Tie points (i.e. homologue point pairs in different images) were marked manually to obtain the relative orientation of the image block. Because of the extremely steep terrain and associated distortions in the aerial images, the usual automatic tie point extraction could barely be applied. The absolute orientation of the image blocks requires the use of GCPs. Because of the lack of survey points on the Monte Rosa east face, the coordinates of GCPs such as buildings and other well-defined immobile surface features were extracted from a topographic map (swisstopo, 1:25 000) and a digital elevation model with 25-m grid spacing (DHM25 Level 2, swisstopo).

The bundle adjustment yielded a high overall accuracy with standard deviation values (σ_0) = 0.48, 0.6 and 0.99 pixels for the different image blocks (Table 2). Using an averaged image scale, this corresponds to about 10–20 cm in object space. The variation of the σ_0 value from 0.48 to 0.99 pixels for 2001 to 1956, respectively, is explained by the better image quality for the more recent aerial images.

The root mean square error (RMSE) value of the control points describes the accuracy of the GCPs and ranges from 0.6 to 2.5 m in planimetry and height (Table 2, XYZ values). This deviation was caused mainly by imprecise GCP coordinates and inaccuracy of the manual point measurements. However, stereo intersection accuracy of the GCPs in image coordinates resulted in half a pixel (Table 2, xy values), which shows the high quality of the orientation given the height and steepness of the rock wall.

DTM Generation.

DTM generation was undertaken in Satellite image Precision Processing (SAT-PP, ETH Zurich), using the exterior orientation parameters recovered in the LPS. The main component of the SAT-PP software package is an enhanced multiple image-matching algorithm for the

Table 2 The σ_0 of the exterior orientation of the three image blocks and RMSE of the control points calculated in LPS.

DTM	σ_0 (Pixel)	Control point RMSE (XYZ in m, xy in pixel)
2001	0.48	X: 1.3, Y: 0.6, Z: 1.5 x: 0.21, y: 0.57
1988	0.60	X: 1.9, Y: 1.3, Z: 2.5 x: 0.15, y: 0.66
1956	0.99	X: 1.6, Y: 1.5, Z: 1.7 x: 0.62, y: 0.34

σ_0 = Total image unit-weight root mean square error. This represents the total RMSE for the triangulation. This standard deviation of the unit weight is a global precision indicator describing the quality of the entire bundle adjustment. XYZ = - Ground coordinates; xy = stereo intersection accuracy of the GCPs in image coordinates. Other abbreviations are given in the text.

extraction of image correspondence and generation of 3D data (Zhang, 2005). The image matching is based on the automatic detection and matching of feature points, grid points and edges (breaklines). Iterative least squares-matching methods are used to achieve precise matches for all the chosen features and for the identification of some false matches (Gruen *et al.*, 2005; Zhang, 2005; Zhang and Gruen, 2006).

In preparation for the automatic point extraction and matching process of the aerial images, seed points were measured manually in each stereo pair of image blocks. For the Monte Rosa east face, ten times more matching points than normal were measured manually because of the complex and steep topography, as well as the extensive ice cover. Point density resulting from the matching process was several points/m² on average, which was as high as the LiDAR point clouds (Table 2). Taking into account the data density and the accuracy of the image triangulation, the final DTM grids were generated at a ground resolution of 2 m.

LiDAR Data Processing.

Processing of the LiDAR raw data, including fitting of the flight lines, and automated as well as manual filtering of ground points, outliers and artefacts, was done by Swissphoto for the 2005 data set and by Helimap System SA for the 2007 data (Luethy and Stengele, 2005; Skalous *et al.*, 2005; Vallet, 2007). The conversion of the processed LiDAR point clouds into a grid raster was done using the SCOP++ (inpho) software (Figure 2). The final DTM grids were generated at a 2-m resolution to allow direct comparison with the photogrammetric DTMs. However, even higher resolutions would be feasible given the point density and distribution of the point cloud.

Co-registration of DTMs.

A direct comparison of multi-temporal DTMs requires the definition of a common reference system to avoid errors due to shifts between the individual DTMs. Due to inaccuracies in the GCPs used and the minimal number of GCPs within the face, the photogrammetrically derived DTMs showed offsets of several metres relative to each other. Consequently, the LiDAR DTM acquired in 2007 was taken as the reference surface for all the other processed DTMs.

Automatic co-registration of the DTMs on the reference DTM was conducted with LS3D (Least Squares 3D Matching software; Akca, 2010). This method estimates the transformation parameters of one DTM relative to the reference using the generalised Gauss-Markoff model, and minimising the sum of squares of the Euclidean distances between the surfaces (Gruen and Akca, 2005). This method is a one-step solution for matching and georeferencing of multiple 3D surfaces. In a first registration step, each DTM was transformed onto the 2007 LiDAR-DTM. Only stable, topographically unchanged surfaces were transformed on the corresponding surfaces of the reference DTM. Five areas of known stable bedrock at least 1000 m² in area and equally distributed over the whole face were manually selected in each DTM. They were subsequently iteratively fitted to the

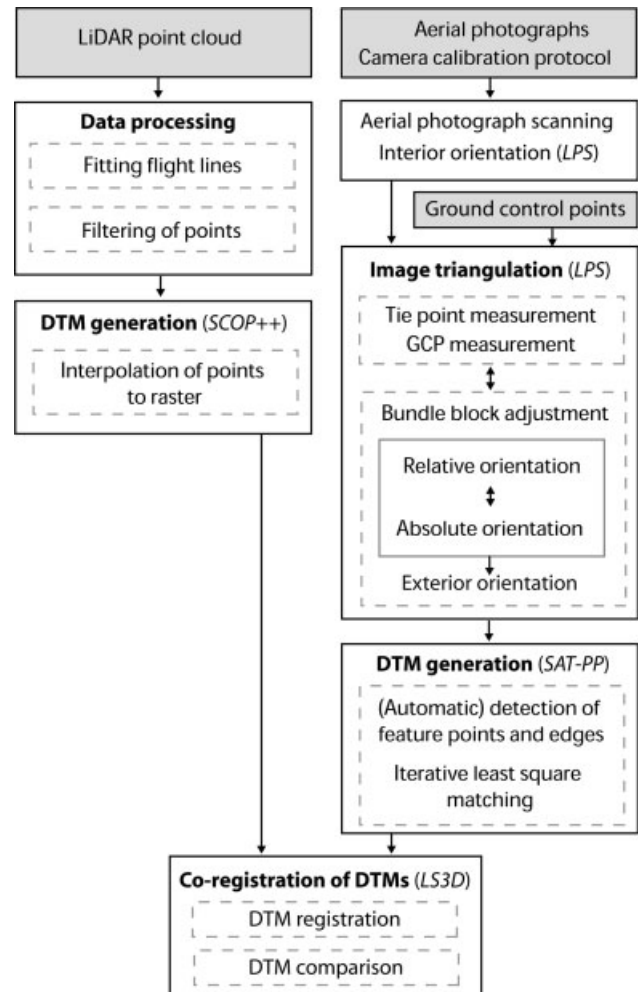


Figure 2 Flow chart of the working steps for data processing. The input data are marked in grey and the software used is shown in italics in brackets (abbreviations as given in the text).

reference DTM by minimising the square sum of distances. In a second step, the difference between the transformed DTMs was calculated (and in the following sections is referred to as 'comparison'). For this DTM comparison, areas with topographic changes were included for the difference calculation.

QUALITY OF THE FINAL DTMS

DTMs From Analogue Aerial Images

The combination of the multi-image-matching approach with intensive manual point matching in SAT-PP enabled the generation of DTMs with a high level of detail, even in this steep and complex terrain (Figure 3, middle left). As a result of feature and line extraction during the image-matching process, linear features were particularly well defined in

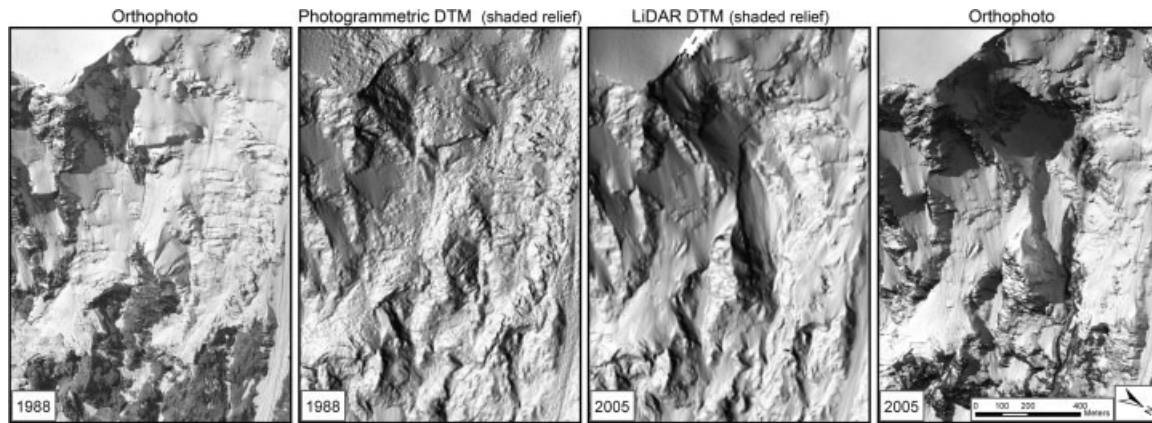


Figure 3 Comparison of the shaded relief models of the 1988 DTM from vertical aerial images (middle left) and the LiDAR DTM from 2005 (Swissphoto, middle right; © BSF Swissphoto). The surface characteristics (glacier or bedrock) can be seen on the corresponding orthophoto (left and right, respectively).

the DTMs. Some drawbacks exist in planar areas, where undulating interference features are visible on bright glacier and snow surfaces (e.g. upper left corner). The problem in these zones is the low radiometric contrast that hinders effective feature, point and edge extraction for the matching process.

LiDAR DTMs

The LiDAR DTMs are highly detailed with the one from 2005 (Figure 3, middle right) showing a very precise reproduction of the topography. The wavelengths of both scanners (1064 nm for Optech and 905 nm for Riegl) allowed scanning of snow and glacier surfaces. However, both data sets showed some gaps in the point cloud which mainly developed due to occlusion during data acquisition in very steep to overhanging zones. These minor gaps could be interpolated during DTM generation. The particularly sound representation of planar segments is clearly a major advantage of the LiDAR technique.

Relative DTM Accuracy

The transformation of all DTMs into the reference coordinate system of the 2007 LiDAR DTM allowed relative accuracy estimation through the registration process. The DTM subtraction implies that individual DTM errors and shifts between DTMs can be combined as independent random variables. Assuming a normal distribution, this combined error can be used as standard deviation σ_0 (Dewitte *et al.*, 2008). For registration based on selected stable areas, the σ_0 of analysed DTMs from the reference DTM lay between 1 m and 2 m (Table 3). Overall, the comparison of photogrammetric DTMs with LiDAR DTMs indicates comparable quality and point density.

The σ_0 of DTM registrations using only topographically unchanged areas can be compared with the σ_0 of DTM comparisons including all topographic changes. The latter were 19.4 m and 16.3 m for the 1956 and 1988 DTMs,

respectively, when compared to the 2007 LiDAR DTM, both much greater than the σ_0 of the corresponding registration, thereby confirming the large topographic changes within these time periods. The σ_0 of comparisons of the 2001 and 2005 DTMs were 4.3 and 2.4 m, respectively, which are much closer to the corresponding registration accuracies (Table 3).

Comparison of e- and z- Distance

Two ways to measure the differences between the surfaces of the DTMs were tried. The z-distance is the vertical elevation difference between corresponding grid cells of two DTMs and is the usual method available in commercial GIS software. The e-distance (Euclidean distance) is the shortest distance between closest located discrete points on two data sets. In uniform or relatively flat terrain, the two distances are similar, but discrepancies may develop in steep or variable terrain (Figure 4).

The z-distance is most commonly applied in geomorphometric studies but is less suitable for quantifying differences in steep areas with slope angles higher than $\sim 50^\circ$ because topographic change can be overestimated (Figure 5). Moreover, even very minor horizontal shifts or errors between DTMs can induce large errors in z-distance values. The e-distance measurement is more suitable for strongly varying and steep topography because the influence of slope angle on surface difference measurements is minimised and

Table 3 The σ_0 of registration and comparison of all DTMs with the 2007 LiDAR DTM.

DTM	σ_0 of registration (m)	σ_0 of comparison (m)
2005	1.6	2.4
2001	1.5	4.3
1988	1.3	16.3
1956	1.9	19.4

Other abbreviations as given in the text.

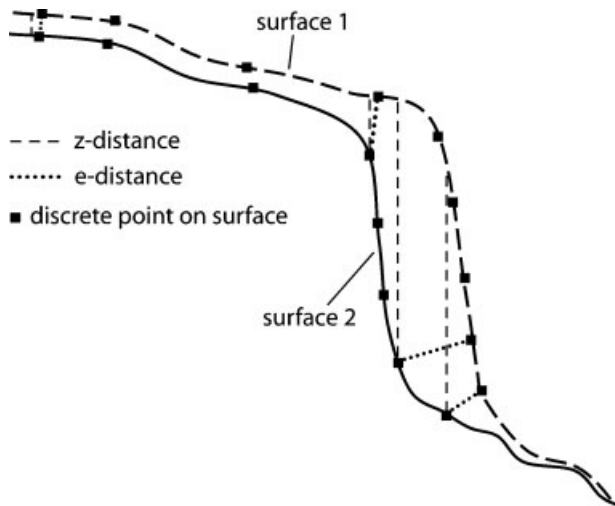


Figure 4 Comparison of z- and e-distance measurements in complex and steep topography. The discrete points are the original measurement points from LiDAR or aerial photogrammetric matching. The e-distance is the line between an individual measurement point and its closest neighbour in the other data set.

accordingly, shifts between DTMs have a much smaller influence. Therefore, the difference calculation in this study was performed using the e-distance.

RESULTS: ANALYSIS OF TOPOGRAPHIC CHANGE

The DTM difference calculations in LS3D yielded a direct estimate of the location and amount of topographic change over the four time periods (Figure 6).

Between 1956 and 1988, very few topographic changes were detected in the bedrock area (Figure 6a). In snow, firn

and ice areas, net accumulation as well as net ablation occurred in equal measure. The e-distance changes averaged about 10 m with a maximum of 30 m in restricted areas. Over 32 years, these correspond to normal processes of volume gain and loss of glaciers as well as moderate rockfall activity on this steep rock wall. This assessment is confirmed by limited change evident on photographs from 1895, 1911, 1983 and 1986 (Figure 7). The large surface differences in area s1 on Figure 6a are caused by local errors in the 1956 DTM as a result of false image matching due to local shadows and poor image quality.

Significantly different patterns developed between 1988 and 2001 that appear to be related to mass movement processes (Figure 6b). Mass loss (glacier ice and bedrock) of up to 115 m occurred in the central part of the face, with a total volume loss exceeding $20 \times 10^6 \text{ m}^3$. Terrestrial photographs from 1986 and 2002 (Figure 7) confirmed the striking changes in the area of the Parete Innominata (upper marking), where a complete hanging glacier and large parts of bedrock disappeared within a few years and a steep rock wall was newly exposed (e1 and e2 in Figure 6b). The temporal resolution of the DTM time series did not allow conclusions to be drawn about the chronology of the topographic changes but interpretations of terrestrial and aerial photographs and observations by local people revealed that the slope failures started after 1988 at the location of e1. Subsequently, the hanging glacier above and the underlying bedrock (marked as e2 in Figure 6b) were lost in a combination of one major and several small-scale rock and ice avalanche events. Interaction between rock avalanche events and glacier retreat caused mass loss further upwards on the face.

In the Imseng Channel (e3 and e4 in Figure 6b), the lowermost part of the glacier disappeared with a mass loss up to 60 m thick between 1999 and 2001. Terrestrial photographs and observations by locals point to a combination of repeated small-scale events and one major

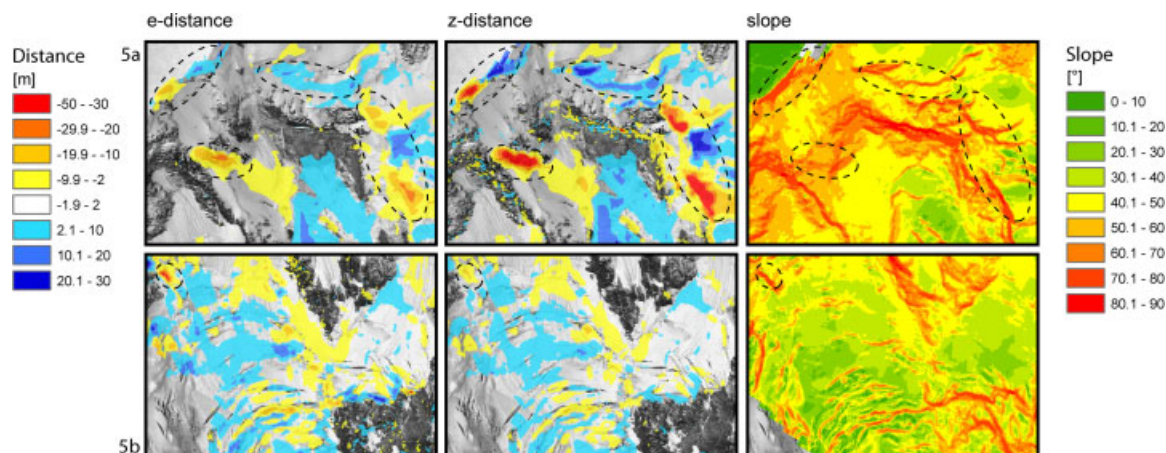


Figure 5 Comparison of DTM subtractions with e- and z-distance measurements. Topographic changes are obtained by the subtraction of the 2005 and 2007 LiDAR DTMs, and slope angles are calculated from the 2005 LiDAR DTM. The upper row shows the DTM comparison for a very steep part of the Monte Rosa east face (marked as 5a in Figure 1), where large differences can be seen between e- and z-distance (marked with black ellipses). In flatter terrain (lower row, 5b in Figure 1), the two measurement methods show similar results.

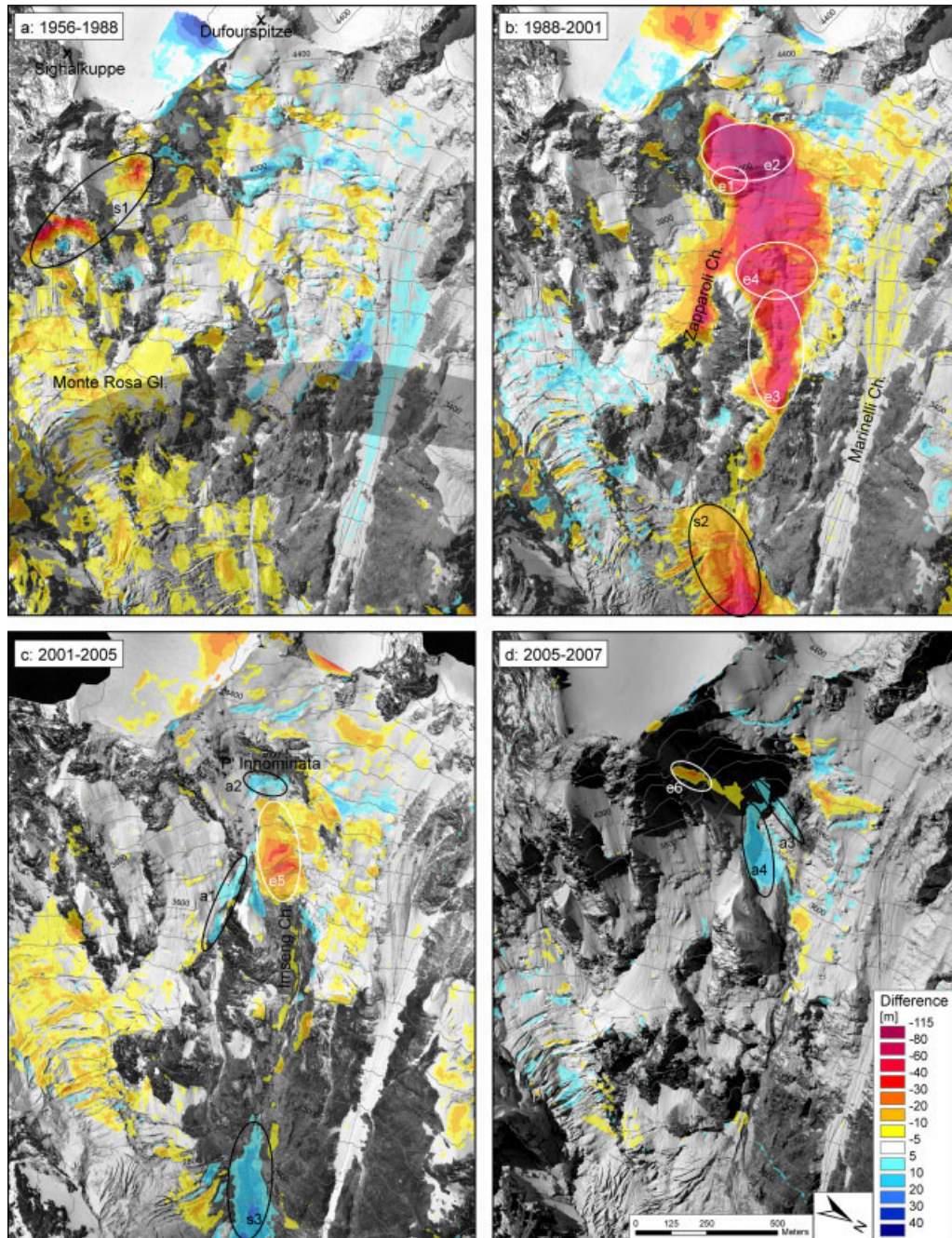


Figure 6 Evolution of the central part of the Monte Rosa east face in the form of e-difference maps for volume loss (red) to volume gain (blue) observed between 1956 and 1988 (a), 1988 and 2001 (b), 2001 and 2005 (c) and 2005 and 2007 (d). There is no shading in areas where apparent change is within ± 5 m. The surface differences are plotted on the orthophotos of 1988 (a and b), 2001 (c) and 2005 (d); the contour interval is 100 m. Significant mass failure events are marked e1 to e6 (e = erosion); zones with striking volume gain are marked a1 to a4 (a = accumulation); special features are marked s1 to s3; explanations are given in the text. The approximate lower limit of the permafrost occurrence is shown in grey in Figure 6a and applies to all graphics.

ice avalanche. The mass failures started in the lowest part of the glacier (e3) and proceeded progressively upwards. This intensive ice avalanche activity combined with rockfall and debris flow activity from newly ice-free areas caused the glacier beneath to be eroded up to 40 m along the runout channel (s2).

Distinct topographic changes again occurred from 2001 to 2005 (Figure 6c). The mass loss in the Imseng Channel (e5) corresponded to a single ice avalanche event in August 2005 with a volume of more than $1 \times 10^6 \text{ m}^3$. This ice avalanche occurred directly above the area where major parts of the glacier detached after 1999 (e3 and e4). Increased rockfall

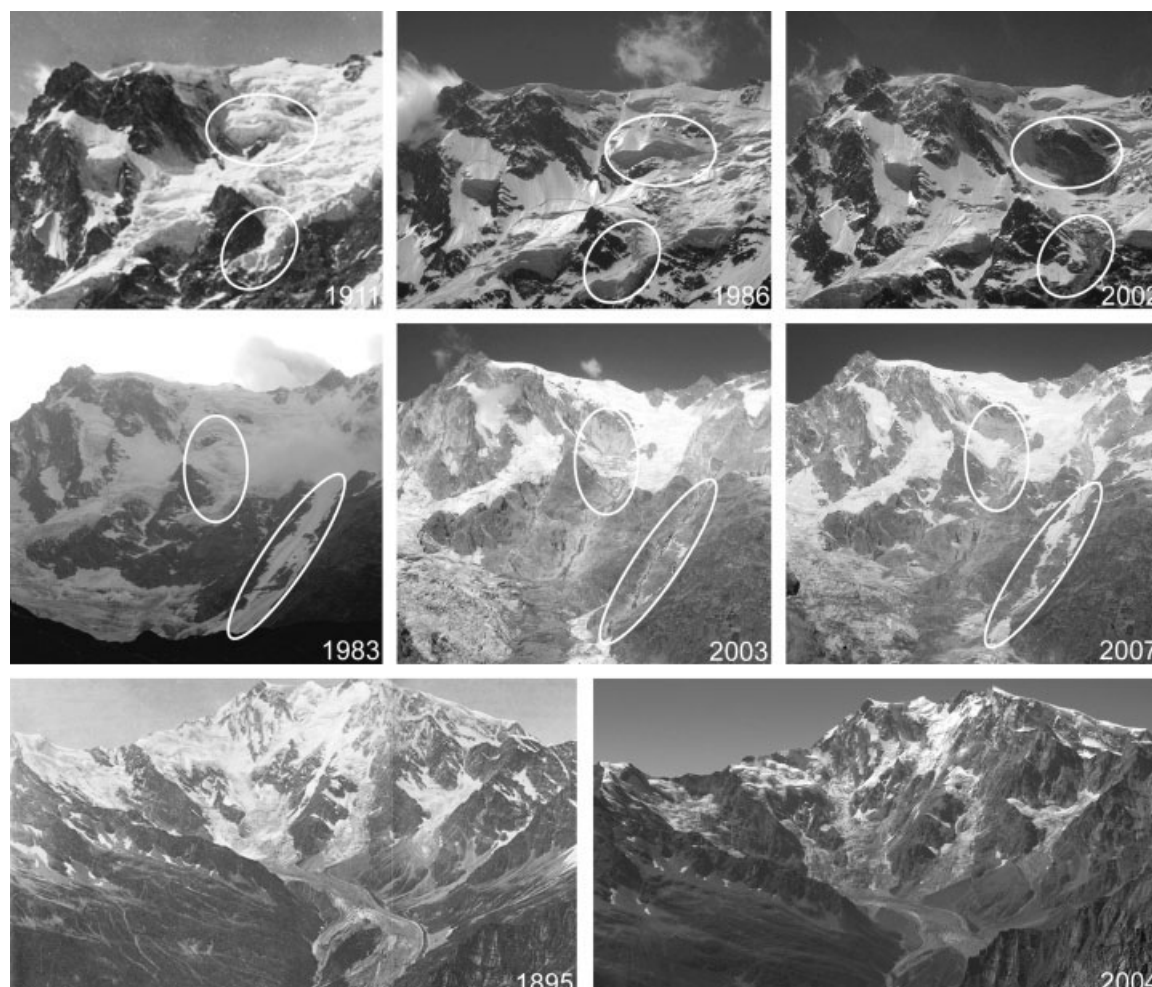


Figure 7 Time series of selected terrestrial photographs of the Monte Rosa east face from 1911 to 2007. The top row shows a detailed view of the upper part of the face, the middle row shows the main face and the bottom row gives an overview of the entire area. The zones with the most significant changes in glaciation and topography are marked in white; for detailed descriptions see the text. The photographs are from: top row: Sella (1911), H. Röthlisberger (1986), W. Haeberli (2002); middle row: W. Haeberli (1983), Fischer (2003, 2007); bottom row: Sella (1895), Fischer (2004).

and debris flow activity just below the glacier front seemed to destabilise the entire glacier. Below the Parete Innominata, a small area of mass gain (a2) developed due to rockfall from the newly ice-free area above. Accumulation of debris and ice also occurred in area s3 where erosion had taken place in 1988–2001. This indicates that the intensity and magnitude of the mass movement activity diminished. Local glacier ice volume gain occurred at site a1 where the main runout channel of mass movements from e1 and e2 was situated before 1999. As this runout channel became inactive due to a shift of rockfall detachment zones, an ice ridge up to 20 m thick built up over the 5 years.

From 2005 to 2007 several distinct topographic changes occurred (Figure 6d). Considerable ice volume gain took place in the Imseng Channel (a4). In the area of the former detachment zone of the 2005 ice avalanche, ice up to 20 m thick accumulated within only 2 years. The detachment zone of the April 2007 rock avalanche is evident (e6) and the difference between the 2005 and 2007 LiDAR DTMs

suggests that the detached rock mass was 15–30 m thick, giving a volume of $0.2 \times 10^6 \text{ m}^3$. The mass loss in the area between e6 and a4 was due to erosion of the ice by the rock avalanche event. Below the Parete Innominata rock wall, mass accumulation is visible at a3, attesting to ongoing small-scale rockfall activity.

DISCUSSION

Data Processing and Final DTMs

LiDAR data collection by helicopter and aeroplane proved to be an invaluable source of detailed, accurate topographic information for terrain that is difficult or impossible to access. High-precision DTM data facilitated detection of topographic changes at metre scale and revealed subtle geomorphic features to an accuracy of 1–3 m. Helicopter-based LiDAR data acquisition is especially advantageous for

relatively small areas (less than about 5 – 10 km²) with high-altitude differences, whereas data acquisition using fixed-wing aircrafts is more suitable for larger areas. However, in such high-mountain environments, several logistical and technical challenges have to be considered for both methods: complicated acquisition geometry, difficult weather conditions (such as strongly varying wind fields and local clouds), limitations of GPS satellite reception and the optimal skills required of the helicopter pilot. Furthermore, the acquisition of aerial LiDAR data is expensive given the need for flying time.

A comparison of the two LiDAR point clouds revealed that while the acquisition geometry of the helicopter-based method perpendicular to the wall intuitively seems to be more suitable, the aeroplane-based method has a denser point distribution with fewer gaps, especially in steep and complex areas. This was due to the ten times higher acquisition rate of the laser scanner used on the aeroplane and greater overlap of the flight lines.

For investigations of time periods before the advent of LiDAR technology, aerial images are the best available quantitative data sources for topographic changes. Aerial images have high spatial resolution and the great advantage of an image record for more than 50 years. However, photogrammetric processing of aerial images is very challenging due to the steepness and low levels of contrast in glaciated areas. The use of a sophisticated photogrammetric processing approach and intensive manual processing permitted for the first time the generation of a highly accurate multi-temporal series of high-resolution DTMs for a large mountain face. This success has to be offset against the time-consuming processing and local errors that remained in the DTMs.

The transformation of individual DTMs to a common reference system using LS3D reduced the offsets between DTMs that were introduced by slightly different GPS positions. These small offsets could have resulted in large DTM differences in steep areas. A solution to eliminate offset errors with the photogrammetric method in the future would be to triangulate aerial images in multi-temporal image blocks, as has been done for matching terrain displacements (Kääb, 2002). Thus, the aerial images of all years could be triangulated in one step with identical GCPs and multi-temporal tie points.

The Euclidean distance (e-distance) proved valuable for reducing errors and misinterpretations in the DTM comparisons. Even using this parameter, however, individual errors can be compounded by DTM subtraction leading to overestimations of topographic change. Therefore, calculated terrain changes should be compared to available aerial and terrestrial photographs.

Periglacial and Glacial Processes

Conclusions about processes affecting slope stability of the east face of Monte Rosa can be drawn from the quantitative assessment in combination with the terrestrial photographs (Figure 7). The quantitative analysis of DTMs reveals

complex patterns of terrain changes, which point to the simultaneous occurrence of different periglacial and glacial processes in a high-mountain face. The following topographic changes could be distinguished and quantitatively assessed:

- rapid mass loss due to frequent small-scale or single large-scale rock and/or ice avalanche events;
- erosion of debris and/or glacier ice in the runout channel by rock and/or ice avalanche events;
- accumulation of debris material from mass movement processes;
- accumulation and ablation of firn and ice over large areas of a steep glacier;
- rapid ice accumulation and build-up of steep glaciers in eroded areas following a major rock or ice avalanche.

The most striking observation is the exceptionally large loss of permafrost-affected bedrock and surface ice of about $20 \times 10^6 \text{ m}^3$ over the entire investigation period. Since about 1990, numerous large rock and ice avalanche events have occurred with no documented historical precedence of similar total magnitude in the European Alps. Moreover, the most recent ice avalanche in 2005 with a volume of more than $1 \times 10^6 \text{ m}^3$ is amongst the largest documented for the European Alps over the past 100 years (Alean, 1985). The volume of this avalanche, however, represents only 5 per cent of the total loss of bedrock and ice. We suspect that such developments indicate major changes relating to permafrost degradation, rapid deglaciation of steep ice masses and associated rock wall stability, which might foreshadow similar processes at other sites.

The DTM comparisons from 1988 to 2007 show that volumetric glacial ice loss or gain can occur much more quickly on a steep face than in a valley glacier. Increased regional ice loss has occurred since 1956 that is probably explained by a 1 °C increase in air temperatures over the last 50 years. However, changes in surface geometry and the size of hanging glaciers can occur independently of climatic conditions (Pralong and Funk, 2006; Post and Lachapelle, 1971). A remarkable phenomenon is the rapid accumulation of ice in distinct zones following erosion by mass movement events or enhanced melting seasons (e.g. in the Zapparoli, Imseng and Marinelli Channels). Such changes in surface ice must also influence the thermal regime of the adjacent bedrock.

A comparison of the slope failure zones (Figure 6) with the modelled permafrost distribution shows that all detachment zones are located in permafrost areas. Firn and glacier ice in these areas are assumed to be mainly cold (Fischer *et al.*, 2006; Huggel, 2009). However, hanging glaciers often have polythermal patterns with sections of much warmer or even temperate firn and ice (e.g. Pralong and Funk, 2006). Such polythermal patterns may locally influence temperatures in the bedrock down to several decametres depth (Wegmann *et al.*, 1998; Huggel, 2009). The small-scale rockfall events, which occurred in the area of the Imseng Channel, the Parete Innominata and elsewhere

in the face, may relate to changes within the near-surface active layer of the permafrost or to enhanced frost weathering after deglaciation. The large-volume rock avalanche of 2007, however, cannot be due only to changes in the thermal subsurface fields. For this event, preceding topographic changes in the surrounding area with a total mass loss of over $15 \times 10^6 \text{ m}^3$ ice and bedrock may have had significant effects on stability by changing the topographic and geomechanical conditions of the remaining bedrock and thereby inducing changes in slope stress fields. At the same time, the response of steep bedrock areas to glacier retreat is strongly conditioned by the geological setting, which in the case of the 2007 event includes a surface-parallel set of bedrock discontinuities that favours instability.

The DTM comparisons and additional imagery analyses revealed that the sequence of topographic changes and slope failures is strongly spatially correlated. The slope failures started in 1990 on a small part of the Parete Innominata with combined rock and ice avalanche activity that induced feedbacks in mass-wasting processes until the whole Parete Innominata and Imseng Channel were ice-free in 2001. Slope instabilities in the permafrost-affected bedrock can diminish the stability of hanging glaciers, and unloading effects due to glacier retreat may induce changed stress fields in the bedrock. As a result of rock or ice avalanches, the terrain may become over-steepened with an altered internal stress field and mass movement activity then occurs to re-establish equilibrium. The analyses show strong stability coupling between permafrost-affected bedrock and adjacent hanging glaciers.

CONCLUSION AND PERSPECTIVES

The results of the multi-temporal DTM comparison in this study represent unprecedented quantitative information on

topographic changes in bedrock and ice in a large periglacial area over half a century. The combination of LiDAR data and photogrammetrically processed aerial images allowed detailed topographic investigations over this lengthy period. Processes that influence glacier and rock slope stability, however, cannot be determined from DTM analyses alone, and the use of orthophotos and terrestrial images as well as additional observations in the field remained essential.

Permafrost and glaciers in cold mountain regions will continue to be affected by climate change. Comparatively strong changes may develop, or have already developed on steep periglacial mountain faces. Consequently, further hazardous situations are likely to emerge. Therefore, remote sensing methods for the investigation and monitoring of high-mountain faces should be further developed and applied. The combination and integration of different technologies help to improve our understanding of processes and aid hazard assessment. The acquisition of LiDAR at regular intervals would be important for establishing a detailed database that documents topographic changes. The installation of automatic cameras taking photographs at high temporal resolution could also provide information for monitoring and hazard assessment.

ACKNOWLEDGEMENTS

We thank H. Röthlisberger, G. Mortara, M. Chiarle, P. Semino and A. Tamburini for providing imagery data and valuable information about the Monte Rosa east face. Special thanks are due to two anonymous referees and A. G. Lewkowicz for detailed and constructive reviews that helped improve this contribution. We acknowledge support and funding from the Swiss National Science Foundation (project no. 200021-111967).

REFERENCES

- Akca D. 2010. Co-registration of surfaces by 3D Least Squares matching. *Photogrammetric Engineering and Remote Sensing* **76**(3): 307–318.
- Alean J. 1985. Ice avalanches: some empirical information about their formation and reach. *Journal of Glaciology* **31**(109): 324–333.
- Allen SK, Gruber S, Owens IF. 2009. Exploring steep bedrock permafrost and its relationship with recent slope failures in the Southern Alps of New Zealand. *Permafrost and Periglacial Processes* **20**: 345–356. DOI: 10.1002/ppp.658.
- Baldi P, Bonvalot S, Briole P, Coltelli M, Gwinner K, Marsella M, Puglisi G, Remy D. 2002. Validation and comparison of different techniques for the derivation of digital elevation models and volcanic monitoring (Vulcano Island, Italy). *International Journal of Remote Sensing* **23**: 4783–4800.
- Baltsavias EP. 1999. A comparison between photogrammetry and laser scanning. *ISPRS Journal of Photogrammetry and Remote Sensing* **54**: 83–94.
- Baltsavias EP, Favey E, Bauder A, Bösch H, Pateraki M. 2001. Digital surface modelling by airborne laser scanning and digital photogrammetry for glacier monitoring. *The Photogrammetric Record* **17**(98): 243–273.
- Barla G, Dutto F, Mortara G. 2000. Brenva Glacier rock avalanche of 18 January 1997 on the Mont Blanc range, northwest Italy. *Landslide news* **13**: 2–5.
- Buchroithner M. 2002. Creating the virtual Eiger North Face. *ISPRS Journal of Photogrammetry and Remote Sensing* **57**(1–2): 114–125.
- Cola G. 2005. The large landslide of the south-east face of Thurwieser peak (Thurwieser-Spitze) 3658 m (Upper Valtellina, Italy). *Terra Glacialis* **8**: 38–45.
- Cox SC, Allen SK. 2009. Vampire rock avalanches of January 2008 and 2003, southern Alps, New Zealand. *Landslides* **6**(2): 161–166.
- Davies MCR, Hamza O, Harris C. 2001. The effect of rise in mean annual temperature on the stability of rock slopes containing ice-filled discontinuities. *Permafrost Periglacial Processes* **12**(1): 137–144. DOI 10.1002/ppp.378.
- Dewitte O, Jasselette J-C, Cornet Y, Van Den Eeckhaut M, Collignon A, Poesen J, Demoulin A. 2008. Tracking landslide displacements by multi-temporal DTMs: *Permafrost and Periglacial Processes*, (2011)

- A combined aerial stereophotogrammetric and LIDAR approach in western Belgium. *Engineering Geology* **99**(1–2): 11–22.
- Evans SG, Clague JJ. 1994. Recent climatic change and catastrophic geomorphic processes in mountain environments. *Geomorphology* **10**: 107–128.
- Fischer L. 2009. Slope instabilities on perennially frozen and glacierised rock walls: multi-scale observations, analyses and modelling. PhD thesis, report no. 58, Physical Geography Division, University of Zurich, Switzerland, 184 pp.
- Fischer L, Kääb A, Huggel C, Noetzli J. 2006. Geology, glacier retreat and permafrost degradation as controlling factors of slope instabilities in a high-mountain rock wall: Monte Rosa east face. *Natural Hazards and Earth System Science* **6**: 761–772.
- Fischer L, Amann F, Moore J, Huggel C. 2010. Assessment of periglacial slope stability for the 1988 Tschierwa rock avalanche (Piz Morteratsch, Switzerland). *Engineering Geology* **116**: 32–43.
- Geertsema M, Clague JJ, Schwab JW, Evans SG. 2006. An overview of recent large catastrophic landslides in northern British Columbia, Canada. *Engineering Geology* **83**: 120–143.
- Gruber S, Haeberli W. 2007. Permafrost in steep bedrock slopes and its temperature-related destabilization following climate change. *Journal of Geophysical Research* **112**: F02S18. DOI: 10.1029/2006JF000547.
- Gruen A, Akca D. 2005. Least squares 3D surface and curve matching. *ISPRS Journal of Photogrammetry and Remote Sensing* **31**(3B): 151–174.
- Gruen A, Zhang L, Eisenbeiss H. 2005. 3D precision processing of high-resolution satellite imagery. In *Proceedings of the ASPRS 2005 Annual Conference*, American Society for Photogrammetry and Remote Sensing, Bethesda, Maryland: Baltimore, Maryland, USA.
- Haeberli W, Wegmann M, Vonder Muehl D. 1997. Slope stability problems related to glacier shrinkage and permafrost degradation in the Alps. *Eclogae Geologicae Helveticae* **90**: 407–414.
- Haeberli W, Kääb A, Paul F, Chiarle M, Mortara G, Mazza A, Deline P, Richardson S. 2002. A surge-type movement at Ghiacciaio del Belvedere and a developing slope instability in the east face of Monte Rosa, Macugnaga, Italian Alps. *Norwegian Journal of Geography* **56**: 104–111.
- Haeberli W, Huggel C, Kääb A, Zraggen-Oswald S, Polkvoj A, Galushkin I, Zotikov I, Osokin N. 2004. The Kolka-Karmadon rock/ice slide of 20 September 2002: an extraordinary event of historical dimensions in North Ossetia, Russian Caucasus. *Journal of Glaciology* **50**(171): 533–546.
- Harris C, Arenson LU, Christiansen HH, Etzelmüller B, Frauenfelder R, Gruber S, Haeberli W, Hauck C, Hoelzle M, Humlum O, Isaksen K, Kääb A, Kern-Lütschg MA, Lehning M, Matsuoka N, Murtin JB, Noetzli J, Phillips M, Ross N, Seppälä M, Springman SM, Vonder Muehl D. 2009. Permafrost and climate in Europe: Monitoring and modelling thermal, geomorphological and geotechnical responses. *Earth Science Reviews* **92**(3–4): 117–171.
- Huggel C. 2009. Recent extreme slope failures in glacial environments: effects of thermal perturbation. *Quaternary Science Reviews* **28**: 1119–1130.
- Huggel C, Zraggen-Oswald S, Haeberli W, Kääb A, Polkvoj A, Galushkin I, Evans SG. 2005. The 2002 rock/ice avalanche at Kolka/Karmadon, Russian Caucasus: assessment of extraordinary avalanche formation and mobility, and application of QuickBird satellite imagery. *Natural Hazards and Earth System Sciences* **5**: 173–187.
- IPCC. 2007. *Climate Change 2007: The Physical Science Basis. Contribution of Working Group I to the Fourth Assessment Report of the Intergovernmental Panel on Climate Change*, Solomon S, Qin D, Manning M, Chen Z, Marquis MC, Averyt K, Tignor M, Miller HL (eds). Intergovernmental Panel on Climate Change: Cambridge and New York.
- Kääb A. 2002. Monitoring high-mountain terrain deformation from repeated air- and spaceborne optical data: examples using digital aerial imagery and ASTER data. *ISPRS Journal of Photogrammetry and Remote Sensing* **57**(1–2): 39–52.
- Kääb A. 2008. Remote sensing of permafrost-related problems and hazards. *Permafrost Periglacial Processes* **19**: 107–136. DOI: 10.1002/ppp.619.
- Kääb A, Huggel C, Barbero S, Chiarle M, Cordola M, Epifani F, Haeberli W, Mortara G, Semino P, Tamburini A, Viazzo G. 2004. Glacier hazards at Belvedere glacier and the Monte Rosa east face, Italian Alps: Processes and mitigation. In *Proceedings of the Interpraevent 2004*. Riva/Trient. I: 67–78.
- Lim M, Petley DN, Rosser NJ, Allison RJ, Long AJ. 2005. Combined digital photogrammetry and time-of-flight laser scanning for monitoring cliff evolution. *The Photogrammetric Record* **20**(110): 109–129.
- Luethy J, Stengele R. 2005. Mapping of Switzerland - challenges and experiences. In *Proceedings of ISPRS WG III/3, III/4, VI/3 Workshop "Laser scanning 2005"*, Enschede, Netherlands, 12–14 September, 2005. 42–47.
- Noetzli J, Hoelzle M, Haeberli W. 2003. Mountain permafrost and recent Alpine rock-fall events: a GIS-based approach to determine critical factors. In *Proceedings of the 8th International Conference on Permafrost*, Phillips M, Springman S, Arenson L (eds). Balkema: Netherlands. 827–832.
- Oppikofer T, Jaboyedoff M, Keusen H-R. 2008. Collapse at the eastern Eiger flank in the Swiss Alps. *Nature Geoscience* **1**: 531–535.
- Pralong A, Funk M. 2006. On the instability of avalanching glaciers. *Journal of Glaciology* **52**(176): 31–48.
- Post A, Lachapelle ER. 1971. *Glacier Ice*. University of Toronto Press: Toronto, Canada. 110 pp.
- Rabatel A, Deline P, Jailliet S, Ravanel L. 2008. Rock falls in high-alpine rock walls quantified by terrestrial lidar measurements: A case study in the Mont Blanc area. *Geophysical Research Letters* **35**(10): L10502. DOI: 10.1029/2008GL033424.
- Ruiz A, Kornus W, Talaya J, Colomer JL. 2004. Terrain modeling in an extremely steep mountain: A combination of airborne and terrestrial lidar. *International Archives of Photogrammetry, Remote Sensing and Spatial Information Sciences* **35**(B3): 281–284.
- Skaloud J, Vallet J, Keller K, Vessière G, Kölbl O. 2005. Helimap: Rapid large scale mapping using handheld LiDAR/CCD/GPS/INS sensors on helicopters. In *Proceedings of the ION GNSS Congress*, Long Beach, California. September 2005.
- Tamburini A, Mortara G. 2005. The case of the "Effimero" Lake at Monte Rosa (Italian Western Alps): studies, field surveys, monitoring. In *Proceedings of the 10th ERB Conference*, Turin, 13–17 October 2004, Unesco, IHP-VI Technical Documents in Hydrology **77**: 179–184.

- Vallet J. 2007. GPS-IMU and LiDAR integration to aerial photogrammetry: Development and practical experiences with Helimap System[®]. Vorträge Dreiländertagung 27. Wissenschaftlich-Technische Jahrestagung der DGPF. 19–21 June 2007, MuttENZ.
- Vallet J, Skaloud J. 2004. Development and experiences with a fully-digital handheld mapping system operated from a helicopter. *International Archives of the Photogrammetry, Remote Sensing and Spatial Information Sciences, ISPRS Congress, Istanbul, Turkey* **35**(B5): 791–796.
- Wang Y, Yang X, Stojic M, Skelton B. 2004. Toward higher automation and flexibility in commercial digital photogrammetric system. *International Archives of the Photogrammetry, Remote Sensing and Spatial Information Sciences* **35**(B2): 838–841.
- Wegmann M, Gudmundsson GH, Haeberli W. 1998. Permafrost changes in rock walls and the retreat of Alpine glaciers: a thermal modelling approach. *Permafrost Periglacial Processes* **9**: 23–33.
- Zraggen A. 2005. Measuring and modeling rock surface temperatures in the Monte Rosa east face. Diploma thesis, ETH Zurich, Switzerland.
- Zhang L. 2005. Automatic digital surface model (DSM) generation from linear array images. PhD thesis, report no. 88, Institute of Geodesy and Photogrammetry, ETH Zurich, Switzerland.
- Zhang L, Gruen A. 2006. Multi-image matching for DSM generation from IKONOS imagery. *ISPRS Journal of Photogrammetry and Remote Sensing* **60**(3): 195–211.
- Züblin M, Fischer L, Eisenbeiss H. 2008. Combining photogrammetry and laser scanning for DEM generation in steep high-mountain areas. *International Archives of the Photogrammetry, Remote Sensing and Spatial Information Sciences* **37**(B6b): 37–43.